

# SCIENTIFIC REPORTS



OPEN

## Assessing the suitability of copper thiocyanate as a hole-transport layer in inverted CsSnI<sub>3</sub> perovskite photovoltaics

Anjana Wijesekara, Silvia Varagnolo , G. Dinesha M. R. Dabera , Kenneth P. Marshall, H. Jessica Pereira  & Ross A. Hatton 

We report the findings of a study into the suitability of copper (I) thiocyanate (CuSCN) as a hole-transport layer in inverted photovoltaic (PV) devices based on the black gamma phase (B- $\gamma$ ) of CsSnI<sub>3</sub> perovskite. Remarkably, when B- $\gamma$ -CsSnI<sub>3</sub> perovskite is deposited from a dimethylformamide solution onto a 180–190 nm thick CuSCN film supported on an indium-tin oxide (ITO) electrode, the CuSCN layer is completely displaced leaving a perovskite layer with high uniformity and coverage of the underlying ITO electrode. This finding is confirmed by detailed analysis of the thickness and composition of the film that remains after perovskite deposition, together with photovoltaic device studies. The results of this study show that, whilst CuSCN has proved to be an excellent hole-extraction layer for high performance lead-perovskite and organic photovoltaics, it is unsuitable as a hole-transport layer in inverted B- $\gamma$ -CsSnI<sub>3</sub> perovskite photovoltaics processed from solution.

Perovskite photovoltaic (PPV) devices using lead (Pb) halides as the light harvesting semiconductor have shown an unprecedented evolution over the span of less than a decade, with the power conversion efficiency increasing from 3.8% in 2009<sup>1</sup> to 22.1% in 2016<sup>2</sup>. However, the possibility of lead contamination of the environment due to failure of the device encapsulants or improper disposal at the end of life is a serious concern for commercial exploitation<sup>3–6</sup>. The latter is because lead is a highly toxic element that accumulates in the food chain<sup>7</sup> and lead perovskites decompose upon exposure to moisture and water to form lead compounds with significant solubility in water<sup>8,9</sup>. Consequently, there is a need for lead-free alternative matched to the needs of photovoltaic (PV) applications. Recent research has shown that tin (Sn) is a potential replacement for Pb in halide perovskites, an element with much lower toxicity than Pb<sup>10</sup>. PPVs based on wholly inorganic tin perovskite PVs are however at a very early stage of development and so to date the highest reported power conversion efficiency is only 6.4%<sup>11</sup>. Much of the dramatic improvement in the power conversion efficiency of lead PPVs has resulted from identification and optimisation of the electron transport layer (ETL) and hole transport layer (HTL)<sup>12</sup> which interface the light harvesting perovskite layer with the electrodes. These interfacial layers are critically important because they: (i) enable the optimization of the light distribution in the device; (ii) facilitate efficient and selective charge extraction, by minimizing the barrier to the extraction of one carrier type, whilst presenting a large barrier to extraction of the charge carriers with opposite polarity carrier; (iii) physically separate the metal electrode from the perovskite layer, blocking the adverse reactions between them.

In the context of Pb-PPVs the doped organic semiconductor spiro-OMeTAD [2,2',7,7'-tetrakis(N,N-di-p-methoxyphenyl-amine)9,9'-spiro-bifluorene] has proved to be the best HTL to date in terms of the device power conversion efficiency<sup>13</sup>. It is however recognized that the high cost and instability of this material will negatively impact the prospects of commercialization and so there is a need to identify lower cost alternative HTLs. In addition to offering long term stability, the charge transport layer at the transparent electrode must also offer high optical transparency, and so there is interest in using wide band gap wholly inorganic HTLs<sup>14</sup> including NiO<sup>15</sup>, CuI<sup>16</sup>, Cs<sub>2</sub>SnI<sub>6</sub><sup>17</sup> and copper (I) thiocyanate (CuSCN)<sup>18–22</sup>. Among these CuSCN has proved to be a particularly effective HTL for high performance Pb-PPVs with both a conventional<sup>12</sup> and inverted device architecture<sup>18</sup>, and also for high performance organic PVs<sup>22</sup>. The success of this material as a HTL is due to its wide band

Department of Chemistry, University of Warwick, CV4 7AL, Coventry, United Kingdom. Correspondence and requests for materials should be addressed to R.A.H. (email: [Ross.Hatton@warwick.ac.uk](mailto:Ross.Hatton@warwick.ac.uk))

gap ( $\geq 3.50$  eV), excellent solution processability at room temperature and high hole-mobility combined with an ionization potential suitable for the efficient extraction of holes<sup>20,22</sup>. Herein, we report the findings of an investigation into the suitability of CuSCN as a HTL in inverted PV devices based on B- $\gamma$ -CsSnI<sub>3</sub>, a semiconductor that is attracting considerable attention because it offers near ideal optoelectronic properties for a single junction PV devices and can be processed at room temperature from dimethylformamide (DMF) solutions of CsI and SnI<sub>2</sub><sup>23</sup>.

In this study diethylsulfide was the solvent of choice for CuSCN deposition because it has been shown to be an excellent solvent for the formation of CuSCN films for electronic applications<sup>18,22</sup>. A solution concentration of 50 mg/ml deposited at room temperature yielded a film thickness of 180–190 nm as measured by step height analysis using atomic force microscopy (AFM): Supporting Information Figure S1. In the first instance these films were used as the HTL in inverted PV devices with the simplified structure: ITO glass| CuSCN| B- $\gamma$ -CsSnI<sub>3</sub> + SnCl<sub>2</sub> (10 mol% excess) |phenyl-C<sub>60</sub>-butyric acid methyl ester (PC<sub>61</sub>BM)|bathocuproine (BCP)|Al. The B- $\gamma$ -CsSnI<sub>3</sub> layer was deposited from DMF solutions at room temperature, with 10 mol% excess SnCl<sub>2</sub> added as a source of excess Sn, according to our previously reported optimized procedure<sup>23</sup>. In a dry nitrogen-filled glovebox CsI, SnI<sub>2</sub> and SnCl<sub>2</sub> were mixed together in 1:1:0.1 molar ratio. To this mixture DMF was added to make an 8 wt% solution (total mass of solids), which was stirred overnight before use. To deposit films, two drops of solution were cast onto a substrate spinning at 4,000 rpm for 60 s. To confirm that DMF is an orthogonal solvent for CuSCN a 180–190 nm thick film of CuSCN was washed with DMF using the same spin-coating procedure as used for perovskite film deposition. The AFM images in Fig. 1(a,b) show that this results in significant smoothing of the surface of the CuSCN because the root-mean-square surface roughness ( $R_q$ ), measured over an area of 10  $\mu\text{m} \times 10 \mu\text{m}$  is reduced from  $\sim 30$  nm before spin casting DMF to  $\sim 10$  nm after washing with DMF by spin casting. This reduction in surface roughness is consistent with partial dissolution of the CuSCN layer during DMF washing and its possible (partial) removal. However, it is clear from Fig. 1(c) that there is no reduction in the intensity of electronic absorption spectrum, which shows that whilst CuSCN is partially dissolved in DMF it is locally redistributed rather than being washed away. The emergence of the shoulder at a wavelength of  $\sim 300$  nm in the absorption spectrum shows that washing with DMF does however significantly improve the crystallinity of the CuSCN film<sup>19</sup>.

B- $\gamma$ -CsSnI<sub>3</sub> perovskite films deposited from 8 wt% DMF solutions by spin coating directly onto CuSCN supported on ITO glass have a high surface coverage with improved uniformity as compared to perovskite films deposited directly onto ITO glass (Fig. 2(d,e) and Supporting Information Figure S2). Measurements of the perovskite film work function made using a Kelvin probe give the same work function for B- $\gamma$ -CsSnI<sub>3</sub> films spun onto freshly cleaned ITO glass and ITO glass coated with 180–190 nm film of CuSCN:  $4.57 \pm 0.01$  eV and  $4.56 \pm 0.02$  eV respectively. The work function of a 180–190 nm thick film of CuSCN on ITO is  $\sim 250$  meV larger at 4.82 eV. These measurements show that the work function of the B- $\gamma$ -CsSnI<sub>3</sub> layer on CuSCN | ITO is consistent with that of B- $\gamma$ -CsSnI<sub>3</sub> only, rather than a complex mixture of B- $\gamma$ -CsSnI<sub>3</sub> and CuSCN. That is, the perovskite film appears to have completely covered the underlying substrate without intermixing of the perovskite and CuSCN layers and its thickness is sufficient for the measured work function to be that of B- $\gamma$ -CsSnI<sub>3</sub>.

It is evident from Fig. 2 that there is no significant difference in the short-circuit current density ( $J_{sc}$ ), open-circuit voltage ( $V_{oc}$ ), fill factor ( $FF$ ) or shape of the external quantum efficiency (EQE) spectrum for PV devices with and without a CuSCN HTL. Given that the CuSCN layer increases the total semiconductor thickness in the device by up to a factor of 5, it is surprising that the  $J_{sc}$  remains unchanged ( $8.1 \text{ mA cm}^{-2}$  vs  $8.2 \text{ mA cm}^{-2}$ ) and the shape of the EQE spectrum remains unchanged, since the light distribution in the device would be significantly changed by the inclusion of such a thick additional layer<sup>24</sup>. It is also unexpected that  $V_{oc}$  for the devices with and without CuSCN; 0.31 V and 0.30 V respectively, is essentially unchanged since the CuSCN layer would be expected to reduce the reverse saturation current by blocking the unwanted extraction of electrons by the ITO electrode, giving rise to an increase in  $V_{oc}$ <sup>21,23</sup>.

Additionally, devices with and without a CuSCN layer improve significantly with storage under nitrogen: Fig. 2 (dashed lines) and Table 1 (red). We have previously shown that this improvement in device performance upon storage under nitrogen is typical of B- $\gamma$ -CsSnI<sub>3</sub> based PV devices without a HTL<sup>23</sup>, and so it is unexpected that PV devices incorporating a CuSCN HTL should exhibit the same evolution in performance with storage.

The simplest explanation for the near identical performance of devices with and without a CuSCN HTL is that there is no change in the energetics at the interface between the perovskite and the ITO electrode and no change in the light distribution within the device, which would require complete displacement of the CuSCN film by the perovskite over layer. To investigate this possibility the electronic absorption spectra of the perovskite and the perovskite|CuSCN bilayer was measured: Fig. 3. It is evident from Fig. 3 that the intense absorbance of CuSCN around 300–350 nm is completely lost after perovskite deposition and the spectrum is identical to that of the perovskite on its own, consistent with complete displacement of the CuSCN layer by the perovskite layer. This experiment was also performed without 10 mol% SnCl<sub>2</sub>, and the result was the same (Figure S3) confirming that SnCl<sub>2</sub> is not responsible for the displacement of the CuSCN layer. To confirm this finding cross-sectional AFM image analysis of scored B- $\gamma$ -CsSnI<sub>3</sub> + 10 mol% SnCl<sub>2</sub> layer and B- $\gamma$ -CsSnI<sub>3</sub> + 10% SnCl<sub>2</sub> | CuSCN bilayer was performed: Fig. 3 (inset) and Supporting Information Figure S4. If the CuSCN and B- $\gamma$ -CsSnI<sub>3</sub> thicknesses were additive, the total combined film thickness would be  $\sim 220$  nm. However, the measured thickness of the bilayer is the same as that of a B- $\gamma$ -CsSnI<sub>3</sub>:SnCl<sub>2</sub> film on its own, consistent with complete displacement of the much thicker underlying CuSCN film.

Corroborating evidence for the complete ejection of the CuSCN layer from the ITO substrate upon perovskite deposition, such that the CuSCN layer is replaced by the perovskite layer is provided by energy dispersive X-ray analysis (EDAX) of the films of CuSCN and B- $\gamma$ -CsSnI<sub>3</sub> + 10 mol% SnCl<sub>2</sub>|CuSCN: Figure S5 and Table S1. In both cases EDAX probes the entire film thickness<sup>25</sup>, as is evident from the intense oxygen and indium peaks in both spectra. The intense Cu and S peaks in the spectrum of CuSCN are completely absent in the bi-layer film, consistent with displacement of the CuSCN film. Further corroborating evidence is provided by X-ray photoelectron

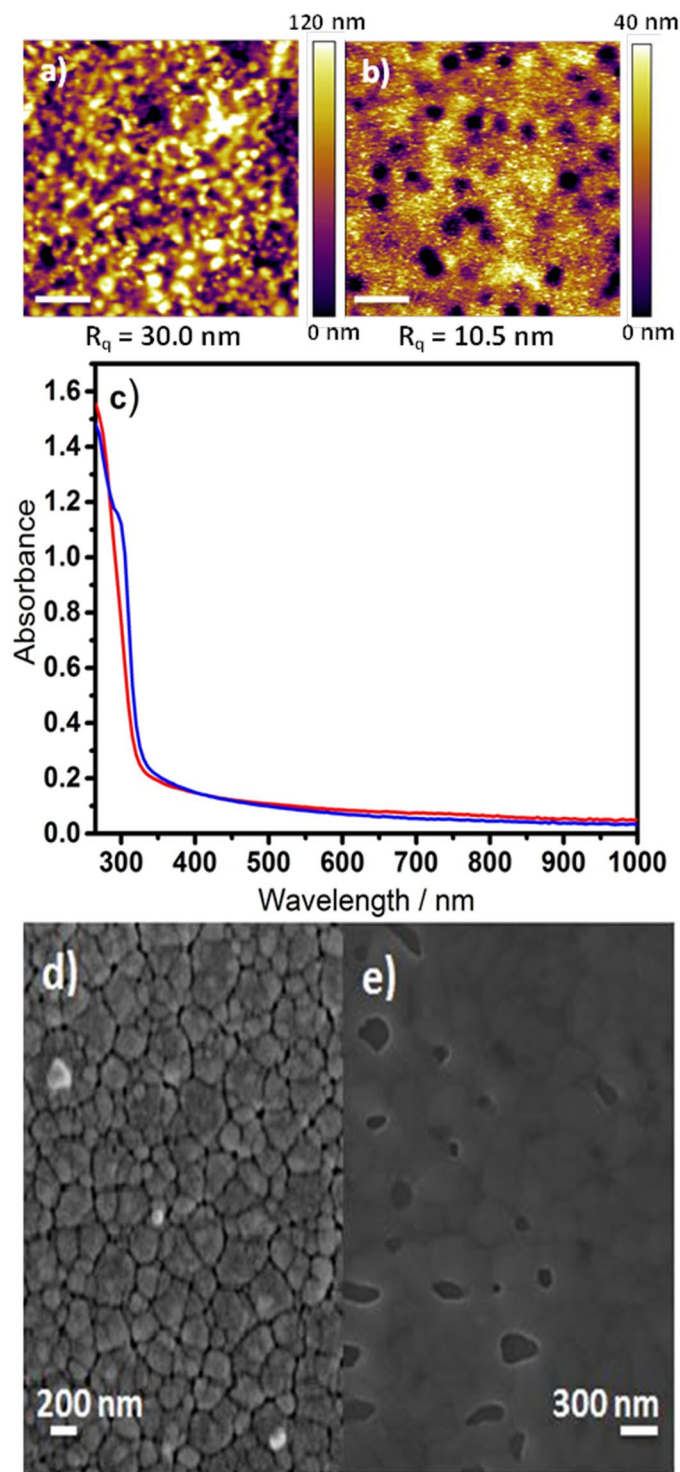


**Figure 1.** (Top): AFM image of surface topography of CuSCN film before (a) and after (b) DMF treatment. (c) Electronic absorption spectra of a spin cast CuSCN film (180–190 nm) on quartz before (red) and after (blue) washing with DMF by spin casting using the same deposition parameters as used for perovskite film deposition. (Bottom): SEM images of B- $\gamma$ -CsSnI<sub>3</sub> + 10 mol% SnCl<sub>2</sub> deposited onto ITO glass with (d) and without (e) a CuSCN layer.

spectroscopy (XPS) analysis (Figure S6) which probes the top 8–10 nm<sup>23</sup> of the perovskite film and any of the underlying substrate exposed at the site of grain boundaries or pinholes. Whilst it is evident from the SEM image in Fig. 2(d) that the perovskite film is compact, there is also a high density of grain boundaries. The indium 3d peaks are clearly resolved in the high resolution (HR) XPS spectrum of the perovskite film deposited onto CuSCN | ITO, with a binding energy consistent with that of ITO<sup>26,27</sup> (Figure S7) confirming that the underlying ITO is

Device	$J_{sc}/(\text{mA cm}^{-2})$	$V_{oc}/\text{V}$	$FF$	$\eta$ (%)	Champion $\eta$ (%)
<b>CuSCN</b>					
n=12	$8.1 \pm 1.1$	$0.31 \pm 0.06$	$0.45 \pm 0.08$	$1.2 \pm 0.5$	1.90
n=12	<b><math>10.1 \pm 1.1</math></b>	<b><math>0.36 \pm 0.01</math></b>	<b><math>0.54 \pm 0.05</math></b>	<b><math>2.0 \pm 0.40</math></b>	<b>2.59</b>
<b>Reference</b>					
n=8	$8.2 \pm 1.1$	$0.30 \pm 0.07$	$0.42 \pm 0.09$	$1.2 \pm 0.6$	1.78
n=7	<b><math>10.1 \pm 0.5</math></b>	<b><math>0.37 \pm 0.02</math></b>	<b><math>0.53 \pm 0.09</math></b>	<b><math>2.2 \pm 0.6</math></b>	<b>2.45</b>

**Table 1.** Average current-voltage ( $JV$ ) parameters for PPV devices ( $\pm$ one standard deviation) with the structure: ITO glass|CuSCN|B- $\gamma$ -CsSnI<sub>3</sub>+10 mol% SnCl<sub>2</sub>|PC<sub>61</sub>BM|BCP|Al, immediately after fabrication (black) and after 28 days storage under nitrogen (bold).

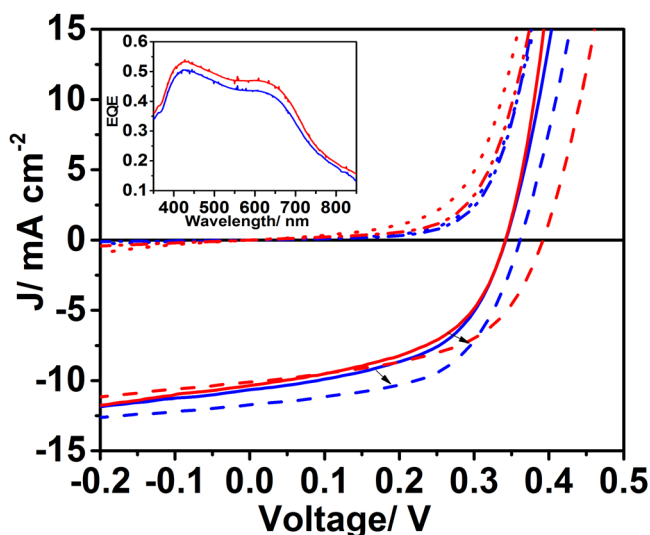


**Figure 2.** Typical current-voltage ( $JV$ ) characteristics for PPVs with the structure: ITO glass|HTL|B- $\gamma$ -CsSnI<sub>3</sub>+10 mol% SnCl<sub>2</sub>|PC<sub>61</sub>BM|BCP|Al, with (blue) and without (red) a CuSCN HTL layer, immediately after fabrication (solid lines) and after 28 days storage under nitrogen (dashed lines). Inset: Typical external quantum efficiency (EQE) spectra for devices with (blue) and without (red) a CuSCN HTL. All device fabrication and testing was performed in a nitrogen filled glovebox ( $<1$  ppm H<sub>2</sub>O and O<sub>2</sub>).

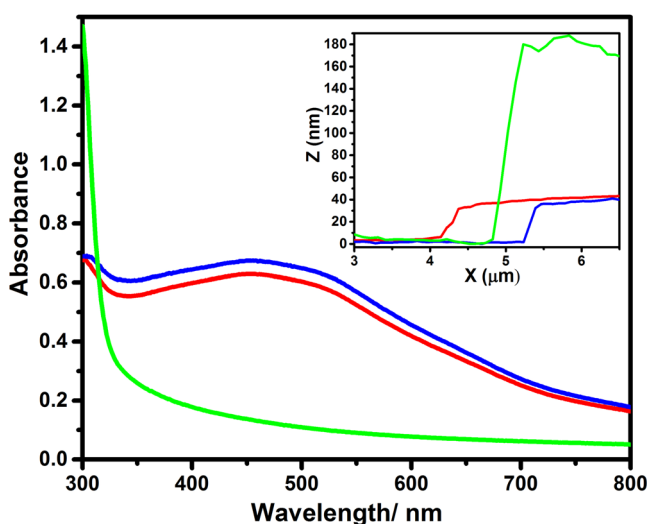


**Figure 3.** Electronic absorption spectra of a B- $\gamma$ -CsSnI<sub>3</sub>+10 mol% SnCl<sub>2</sub> film on: glass (red); a bilayer of B- $\gamma$ -CsSnI<sub>3</sub>+10 mol% SnCl<sub>2</sub>|CuSCN on glass (blue); a CuSCN film on glass (green). Inset: Representative AFM image step edge profiles of: B- $\gamma$ -CsSnI<sub>3</sub>+10 mol% SnCl<sub>2</sub> (red); a bilayer of B- $\gamma$ -CsSnI<sub>3</sub>+10 mol% SnCl<sub>2</sub>|CuSCN (blue); a CuSCN film (green). A statistical analysis of the step edges in scored films is given in Supplementary Information Figure S4.

probed using this technique. The complete absence of Cu, N and S in the HR-XPS spectra (Figure S6) is consistent with the complete displacement of the CuSCN upon spin casting the perovskite layer. Additionally, X-ray diffraction (XRD) analysis confirms this conclusion, since there is no overlap between the powder patterns of the bilayer and CuSCN (Figure S8) and all of the reflections in the XRD pattern of the bilayer can be assigned to the simulated pattern of B- $\gamma$ -CsSnI<sub>3</sub>.<sup>28</sup>

To test the generality of this finding we have also considered the case of using dimethyl sulfoxide (DMSO) as the solvent for perovskite film deposition. Notably, unlike for DMF, B- $\gamma$ -CsSnI<sub>3</sub> perovskite does not form directly from DMSO solutions at room temperature, but there is rapid crystallization to form a solvated intermediate<sup>29</sup> which must be annealed for conversion to the perovskite. Figure S9 shows the electronic absorption spectra of the perovskite and the perovskite|CuSCN bilayer, from which it is evident that the intense absorbance of CuSCN around 300–350 nm is completely lost after perovskite deposition, and the spectrum is essentially identical to that of the perovskite only. This conclusion is supported by EDAX analysis of CuSCN film before and after deposition of the perovskite onto the CuSCN film: In the EDAX spectrum of the bilayer (Figure S10) the Cu and S peaks are absent, or at the resolution limit. Corroborating evidence is provided by the XPS analysis of the bilayer deposited from DMSO given in (Figure S11), which shows that Cu, S and N are not present in the film. The presence of intense In 3d peaks with binding energies consistent with ITO<sup>30</sup> environment (Figure S12) shows that the underlying substrate is visible to this technique, consistent with the large gaps between crystallites seen in the SEM image of the film (Figure S13). Taken together the experimental evidence therefore shows that the 180–190 nm CuSCN layer is completely by the perovskite film during the deposition process, just as when DMF is used as the solvent.

The complete displacement of the 180–190 nm thick CuSCN film by the perovskite film (which in this case is also only one quarter of the thickness of the CuSCN film) is remarkable, not least because of the high speed of film formation during spin-casting. This finding is attributed to a combination of the increased solvation power of DMF and DMSO for CuSCN, due to the high ionic strength associated with halide and metal ions, together with the tendency for very rapid crystallization either directly to the B- $\gamma$ -CsSnI<sub>3</sub> perovskite or a solvated intermediate<sup>29</sup>. Tin perovskites are known to crystallize much more rapidly than their lead analogues due to the high Lewis acidity of Sn<sup>2+</sup><sup>30</sup>, and the enthalpy of formation of the B- $\gamma$ -CsSnI<sub>3</sub> perovskite is very low as compared to that of CuSCN ( $\sim 0.06$  eV<sup>31</sup> vs 1.14 eV<sup>32</sup>), so the process of complete ejection of the CuSCN under layer is evidently a strongly kinetically driven process.

In conclusion, whilst CsSCN has proved to be a low cost HTL for Pb-PPV and high performance organic PVs, here we have shown that is unsuitable as a HTL in solution processed B- $\gamma$ -CsSnI<sub>3</sub> based PPV with an inverted device architecture. Unencapsulated PPV based on B- $\gamma$ -CsSnI<sub>3</sub> with an inverted architecture have been shown to exhibit promising device stability<sup>23</sup>, although the power conversion efficiency has remained stubbornly low primarily due to a low  $V_{oc}$ . The ionization potential of B- $\gamma$ -CsSnI<sub>3</sub> is particularly small amongst tin and lead halide perovskites<sup>33</sup> and so in order to achieve a significantly increased  $V_{oc}$ , energetic losses that occur during hole-extraction must be minimized. The identification of a suitable HTL layer, which has hitherto proved elusive<sup>31</sup>, is therefore essential to improve the efficiency of B- $\gamma$ -CsSnI<sub>3</sub> based PPVs, and so represents a fertile area of research.

## Methods

**CuSCN film deposition.** A solution concentration of 50 mg/ml CuSCN in diethyl sulfide was drop cast onto a freshly cleaned ITO glass substrate spinning at 3000 rpm for 60 seconds.

**B- $\gamma$ -CsSnI<sub>3</sub> film deposition.** In a dry nitrogen-filled glovebox CsI, SnI<sub>2</sub> and tin(II) halide were mixed together in 1:1:0.1 molar ratio. To this mixture N,N-dimethylformamide (DMF) was added to make an 8 wt% solution (total mass of solids), which was stirred overnight before use. To deposit films, two drops of solution were cast onto the substrate (sufficient to cover the whole substrate), followed by spinning at 4,000 r.p.m. for 60 s. The B- $\gamma$ -CsSnI<sub>3</sub> phase forms immediately upon solvent evaporation.

**Device fabrication.** Indium tin oxide (ITO) coated glass slides (Thin Films Devices Inc.  $15 \pm 3 \Omega \text{ sq}^{-1}$ .) were held in vertical slide holders and ultrasonically agitated in an acetone bath, followed by a high purity water bath with a few drops of surfactant, followed by high purity deionized water only bath, acetone and finally an isopropanol bath. Slides were then UV/O<sub>3</sub> treated for 15 minutes. Immediately after UV/O<sub>3</sub> treatment the slides were transferred into a dry nitrogen filled glovebox for CuSCN film deposition followed by deposition of the perovskite and finally the PC<sub>61</sub>BM layer from 13 mg ml<sup>-1</sup> chlorobenzene solution using a spin speed of 1500 rpm. This was followed by thermal evaporation of 6 nm bathocuproine (BCP) deposited at 0.5 Å s<sup>-1</sup> and then 60 nm of Al deposited at 1 Å s<sup>-1</sup>. Thermal evaporation was performed at a pressure of  $1 \times 10^{-5}$  mbar with substrate rotation. The Al electrode was deposited through a shadow mask to make six devices per slide, each with an area of 6 mm<sup>2</sup>.

**PV device testing.** Device testing was performed in the same glove box as used for device fabrication using a solar simulator inside the glove box. Current density–voltage ( $J$ – $V$ ) curves were measured using a Keithley 2400 source-meter under AM1.5 G solar illumination at 100 mW cm<sup>2</sup> (1 sun), scanned from 1 V to +1 V at 0.1 Vs<sup>-1</sup>. External quantum efficiency (EQE) measurements were carried out using a Scientech SF150 xenon arc lamp and a PTI monochromator, with the monochromatic light intensity calibrated using a Si photodiode (Newport 818-UV). The incoming monochromatic light was chopped at 180 Hz. For signal measurement a Stanford Research Systems SR 830 lock-in amplifier was used.  $J$ – $V$  and EQE measurements were made using custom LabVIEW programs.

**Electronic absorption spectroscopy.** Ultraviolet/visible/near-infrared spectra were measured for optically thin films of CuSCN, B- $\gamma$ -CsSnI<sub>3</sub> and bilayer of CuSCN B- $\gamma$ -CsSnI<sub>3</sub> on glass or quartz substrates.

**Atomic force microscopy (AFM).** AFM imaging was performed in tapping mode using an Asylum Research MFP – 3D to determine the step height of the films and morphologies.

**Scanning electron microscopy (SEM).** SEM imaging was performed using a Zeiss SUPRA 55VP field emission gun SEM.

**X-ray photoelectron spectroscopy (XPS).** XPS analysis was performed using a Kratos AXIS Ultra DLD. Samples were unavoidably exposed to air for approximately 1 min during transfer from an air-tight box to the vacuum chamber of the instrument. XPS measurements were carried out in an ultrahigh vacuum system with a base pressure of  $5 \times 10^{-11}$  mbar. The sample was excited with X-rays from a monochromated Al K $\alpha$  source ( $h\nu = 1,486.7$  eV), with the photoelectrons being detected at a 90° take-off angle. The sputtering was carried out at room temperature using a Minibeam I ion gun (Kratos Analytical). A beam of 4 keV Ar<sup>+</sup> ions was incident on a  $3 \times 3$  mm area of the sample surface. Curve fitting was performed using the CasaXPS package, incorporating Voigt (mixed Gaussian Lorentzian) line shapes and a Shirley background.

**X-ray diffraction (XRD).** XRD was performed on thin films of CuSCN prepared from diethyl sulphide solution and a bilayer of CuSCN and B- $\gamma$ -CsSnI<sub>3</sub> prepared from 8 wt% (total solids) DMF solution deposited onto a glass substrate ( $13 \times 13$  mm<sup>2</sup>) spinning at 4000 rpm for 60 seconds. Measurements were made on a Panalytical X'Pert Pro MRD equipped with an Anton Paar DHS 1100 domed stage under a flow of N<sub>2</sub>. Simulated diffraction patterns were calculated using the program Mercury 3.122 using CIFs from the Inorganic Crystal Structure Database (ICSD).

## Data Availability

All data supporting this study are provided as supplementary information accompanying this paper.

## References

- Kojima, A., Teshima, K., Shirai, Y. & Miyasaka, T. Organometal halide perovskites as visible-light sensitizers for photovoltaic cells. *J. Am. Chem. Soc.* **131**, 6050–6051 (2009).
- Hoefler, S. F., Trimmel, G. & Rath, T. Progress on lead-free metal halide perovskites for photovoltaic applications: a review. *Monatshfte fur Chemie.* **148**, 795–826 (2017).
- Li, M., Gou, H., Al-Ogaidi, I. & Wu, N. Nanostructured sensors for detection of heavy metals: A review. *ACS Sustain. Chem. Eng.* **1**, 713–723 (2013).
- Flora, G., Gupta, D. & Tiwari, A. Toxicity of lead: A review with recent updates. *Interdiscip. Toxicol.* **5**, 47–58 (2012).
- EFSA CONTAM Panel. European Food Safety Authority. Scientific Opinion on Lead in Food. *EFSA J.* **13**, 1–321 (2015).
- Giustino, F. & Snaith, H. J. Toward Lead-Free Perovskite Solar Cells. *ACS Energy Lett.* **1**, 1233–1240 (2016).
- Babayigit, A., Ethirajan, A., Muller, M. & Conings, B. Toxicity of organometal halide perovskite solar cells. *Nat. Mater.* **15**, 247–251 (2016).
- Niu, G. *et al.* Study on the stability of CH<sub>3</sub>NH<sub>3</sub>PbI<sub>3</sub> films and the effect of post-modification by aluminum oxide in all-solid-state hybrid solar cells. *J. Mater. Chem. A.* **2**, 705–710 (2014).
- Huang, W., Manser, J. S., Kamat, P. V. & Ptasinska, S. Evolution of Chemical Composition, Morphology, and Photovoltaic Efficiency of CH<sub>3</sub>NH<sub>3</sub>PbI<sub>3</sub> Perovskite under Ambient Conditions. *Chem. Mater.* **28**, 303–311 (2016).
- Tan, H. *et al.* Efficient and stable solution processed planar perovskite solar cell via contact passivation. *Science.* **355**, 722–726 (2017).
- Noel, N. K. *et al.* Lead-free organic–inorganic tin halide perovskites for photovoltaic applications. *Energy Environ. Sci.* **7**, 3061–3068 (2014).
- Arora, N. *et al.* Perovskite solar cells with CuSCN hole extraction layers yield stabilized efficiencies greater than 20%. *Science* **358**, 768–771 (2017).
- Liu, M., Johnston, M. B. & Snaith, H. J. Efficient planar heterojunction perovskite solar cells by vapour deposition. *Nature.* **501**, 395–398 (2013).
- Pattanasattayavong, P. *et al.* Electric field-induced hole transport in copper(i) thiocyanate (CuSCN) thin-films processed from solution at room temperature. *Chem. Commun.* **49**, 4154–4156 (2013).
- Chen, W. & Chen, H. Efficient and stable large-area perovskite solar cells with inorganic charge extraction layers. *Science.* **350**, 1–6 (2015).
- Christians, J. A., Fung, R. C. M. & Kamat, P. V. An inorganic hole conductor for Organo-lead halide perovskite solar cells. improved hole conductivity with copper iodide. *J. Am. Chem. Soc.* **136**, 758–764 (2014).
- Lee, B. *et al.* Air-stable molecular semiconducting iodosalts for solar cell applications: Cs<sub>2</sub>SnI<sub>6</sub> as a hole conductor. *J. Am. Chem. Soc.* **136**, 15379–15385 (2014).
- Treat, N. D. *et al.* Copper thiocyanate: An attractive hole transport/extraction layer for use in organic photovoltaic cells. *Appl. Phys. Lett.* **13301**, 3–8 (2016).
- Wijeyasinghe, N. & Anthopoulos, T. D. Copper(I) thiocyanate (CuSCN) as a hole-transport material for large-area opto/electronics. *Semicond. Sci. Technol.* **30** (2015).
- Pattanasattayavong, P., Promarak, V. & Anthopoulos, T. D. Electronic Properties of Copper(I) Thiocyanate (CuSCN). *Adv. Electron. Mater.* **3** (2017).
- Chaudhary, N., Chaudhary, R., Kesari, J. P., Patra, A. & Chand, S. Copper thiocyanate (CuSCN): an efficient solution-processable hole transporting layer in organic solar cells. *J. Mater. Chem. C.* **3**, 11886–11892 (2015).
- Yaacobi-Gross, N. *et al.* High-efficiency organic photovoltaic cells based on the solution-processable hole transporting interlayer copper thiocyanate (CuSCN) as a replacement for PEDOT:PSS. *Adv. Energy Mater.* **5**, 1–7 (2015).
- Marshall, K. P., Walker, M., Walton, R. I. & Hatton, R. A. Enhanced stability and efficiency in hole-transport-layer-free CsSnI<sub>3</sub> perovskite photovoltaics. *Nat. Energy.* **1**, 1–9 (2016).
- Armin, A. *et al.* Electro-Optics of Conventional and Inverted Thick Junction Organic Solar Cells. *ACS Photonics* **2**, 1745–1754 (2015).
- Amari, H., Ross, I. M., Wang, T. & Walther, T. Characterization of InGaN/GaN epitaxial layers by aberration corrected TEM/STEM. *Phys. Status Solidi Curr. Top. Solid State Phys.* **9**, 546–549 (2012).
- Dobson, P., Salata, V. & Egdell, R. G. High resolution x-ray photoemission study of plasma oxidation of indium – tin – oxide thin film surfaces. *J. Appl. Phys.* **88**, 5180–5187 (2000).

27. Jouad, Z. E., Louarn, G., Praveen, T., Predeep, P. & Cattin, L. Improved electron collection in fullerene via caesium iodide or carbonate by means of annealing in inverted organic solar cells. *EPJ Photovoltaics*. **5**, 50401–50408 (2014).
28. Chung, I. *et al.* CsSnI<sub>3</sub>: Semiconductor or Metal? High Electrical Conductivity and Strong Near-Infrared Photoluminescence from a Single Material. High Hole Mobility and Phase-Transitions. *J. Am. Chem. Soc.* **134**, 8579–8587 (2012).
29. Hao, F. *et al.* Solvent-Mediated Crystallization of CH<sub>3</sub>NH<sub>3</sub>SnI<sub>3</sub> Films for Heterojunction Depleted Perovskite Solar Cells. *J. Am. Chem. Soc.* **137**, 11445–11452 (2015).
30. Thøgersen, A., Rein, M., Monakhov, E. & Mayandi, J. Elemental distribution and oxygen deficiency of magnetron sputtered indium tin oxide films. *J. Appl. Phys.* **109**, 113532 (2015).
31. Marshall, K. P. *et al.* Cs<sub>1-x</sub>Rb<sub>x</sub>SnI<sub>3</sub> light harvesting semiconductors for perovskite photovoltaics. *Mater. Chem. Front.* **2**, 1515–1522 (2018).
32. Jaffe, J. E. *et al.* Electronic and Defect Structures of CuSCN. *J. Phys. Chem. C*. **114**, 9111–9117 (2010).
33. Marshall, K. P., Walker, M., Walton, R. I. & Hatton, R. A. Elucidating the role of the hole-extracting electrode on the stability and efficiency of inverted CsSnI<sub>3</sub>/C<sub>60</sub> perovskite photovoltaics. *J. Mater. Chem. A*. **5**, 21836–21845 (2017).

## Acknowledgements

The authors would like to thank the United Kingdom Engineering and Physical Sciences Research Council (EPSRC) for funding (Grant Number: EP/N009096/1 and EP/L505110/1), the Leverhulme Trust (RPG-2015-044) and the University of Warwick for the award of a Chancellor's International Scholarship to Anjana Wijesekara.

## Author Contributions

A.W. designed all of the experiments, and performed all experiments except XRD, XPS and EDAX, analyzed the data from all experiments and wrote the manuscript. S.V. collected the XPS and EDAX data and helped with data analysis. G.D.M.R.D. collected the XRD data. K.P.M. fabricated some of the preliminary photovoltaic devices. H.J.P. helped analyze the XPS and AFM data. R.H. conceived the study and co-wrote the manuscript.

## Additional Information

**Supplementary information** accompanies this paper at <https://doi.org/10.1038/s41598-018-33987-7>.

**Competing Interests:** The authors declare no competing interests.

**Publisher's note:** Springer Nature remains neutral with regard to jurisdictional claims in published maps and institutional affiliations.



**Open Access** This article is licensed under a Creative Commons Attribution 4.0 International License, which permits use, sharing, adaptation, distribution and reproduction in any medium or format, as long as you give appropriate credit to the original author(s) and the source, provide a link to the Creative Commons license, and indicate if changes were made. The images or other third party material in this article are included in the article's Creative Commons license, unless indicated otherwise in a credit line to the material. If material is not included in the article's Creative Commons license and your intended use is not permitted by statutory regulation or exceeds the permitted use, you will need to obtain permission directly from the copyright holder. To view a copy of this license, visit <http://creativecommons.org/licenses/by/4.0/>.

© The Author(s) 2018